# Identification of a stereotypic molecular arrangement of glycine receptors at native spinal cord synapses

**Stephanie A Maynard[1], Philippe Rostaing[1], Olivier Gemin[1], Adrien Candat[1], Andréa Dumoulin[1], Natascha Schaefer[2], Carmen Villmann[2], Antoine Triller[1]*, Christian G Specht[1,3]***

[1] Institut de Biologie de l'ENS (IBENS), Ecole Normale Supérieure, CNRS, Inserm, Université PSL, Paris, France

[2] Institute for Clinical Neurobiology, University Hospital, Julius-Maximilians-University, Würzburg, Germany

[3] Diseases and Hormones of the Nervous System (DHNS), Inserm, Université Paris-Saclay, Le Kremlin-Bicêtre, Paris, France

* correspondence: triller@biologie.ens.fr, christian.specht@inserm.fr

**ORCID numbers:**

Stephanie A Maynard 0000-0002-7838-3676

Olivier Gemin 0000-0003-3210-7876

Andréa Dumoulin 0000-0003-1309-3448

Natascha Schaefer 0000-0001-9743-1963

Carmen Villmann 0000-0003-1498-6950

Antoine Triller 0000-0002-7530-1233

Christian G Specht 0000-0001-6038-7735

**Short title:**

Quantitative SR-CLEM of glycinergic synapses

**Key words**

single molecule localization microscopy (SMLM); glycine receptor (GlyR); gephyrin; photoactivated localization microscopy (PALM); correlative light and electron microscopy (CLEM); super-resolution CLEM (SR-CLEM); super-resolution radial fluctuation (SRRF) analysis; spinal cord; synapse; hyperekplexia; oscillator mouse model; hypomorph

## Abstract

Precise quantitative information about the molecular architecture of synapses is essential to understanding the functional specificity and downstream signaling processes at specific populations of synapses. Glycine receptors (GlyRs) are the primary fast inhibitory neurotransmitter receptors in the spinal cord and brain stem. These inhibitory glycinergic networks crucially regulate motor and sensory processes. Thus far the nanoscale organization of GlyRs underlying the different network specificities has not been defined. Here, we have quantitatively characterized the molecular arrangement and ultra-structure of glycinergic synapses in native spinal cord tissue using quantitative super-resolution correlative light and electron microscopy (SR-CLEM). We show that GlyRs exhibit equal receptor-scaffold occupancy and constant absolute packing densities of about 2000 GlyRs $\mu m^{-2}$ at synapses across the spinal cord and throughout adulthood, even though ventral horn synapses have twice the total copy numbers, larger postsynaptic domains and more convoluted morphologies than dorsal horn synapses. We demonstrate that this stereotypic molecular arrangement is maintained at glycinergic synapses in the *oscillator* mouse model of the neuromotor disease hyperekplexia despite a decrease in synapse size, indicating that the molecular organization of GlyRs is preserved in this hypomorph. We thus conclude that the morphology and size of inhibitory PSDs rather than differences in GlyR packing determine the postsynaptic strength of glycinergic neurotransmission in motor and sensory spinal cord networks.

## Introduction

Synaptic transmission relies on the integration of neurotransmitter-induced signals by membrane receptors in the postsynaptic density (PSD). The molecular arrangement of postsynaptic receptors and scaffold proteins is therefore key to the synaptic function, however the heterogeneity and complexity of the PSD has made it difficult to resolve its internal organization, to ascertain whether distinct compositional states exist, and to determine how the organization is affected in disease.

Glycine receptors (GlyRs) are the main inhibitory neurotransmitter receptors in the adult spinal cord and brainstem. Glycinergic neurons arise from different embryonic origins, with specific types of neurons residing in characteristic layers of the spinal cord (Lu et al., 2015). Depending on their location, glycinergic neurons mediate sensory and motor information in the dorsal and ventral spinal cord, respectively, which requires high reliability and fidelity of

transmission (Alvarez, 2017). Consequently, deficits in glycinergic transmission are involved in pain mechanisms (Harvey et al., 2004) and motor-related neurological diseases (Schaefer et al., 2018). The electrophysiological properties of glycinergic currents indicate that only a limited number of receptors are activated by the release of a single synaptic vesicle (Oleskevich et al., 1999; Singer and Berger, 1999), suggesting that the nanoscale organization of the receptors determines signal amplitude.

It has been shown that neurotransmitter receptors at excitatory and inhibitory GABAergic synapses are organized within sub-synaptic domains (SSDs) that are aligned with presynaptic elements of the active zone (AZ) (Crosby et al., 2019; MacGillavry et al., 2013; Pennacchietti et al., 2017; Tang et al., 2016). These so-called trans-synaptic nanocolumns are thought to increase the efficacy of synaptic transmission (Haas et al., 2018). At mixed inhibitory synapses, both glycine and $GABA_A$ receptors are immobilized opposite to presynaptic release sites through direct interactions with their common scaffold protein gephyrin (Maric et al., 2011; Specht et al., 2013). However, absolute quantification of receptor numbers and their precise arrangement within the native PSD is lacking. Further, the question is raised as to whether the structure of glycinergic synapses varies in functionally diverse circuits of the dorsal and ventral spinal cord, if it changes over time such as aging, and if it is disturbed in GlyR pathologies such as the neuromotor disease hyperekplexia in humans. In these patients, mutations within the receptor subunit genes *GLRA1* and *GLRB* lead to decreased receptor availability and disturbances in glycinergic transmission, causing exaggerated startle reflexes, muscle hypertonia and stiffness in infancy (Chung et al., 2013; Chung et al., 2010; Schaefer et al., 2013).

To investigate whether the molecular arrangement of GlyRs may account for differences in the functional specificity of sensory and motor circuits we have quantitatively analyzed the ultra-structural organization of inhibitory synapses in native tissue. We have combined molecule counting of endogenous GlyRs using single molecule localization microscopy (SMLM) with correlative light and electron microscopic analysis (CLEM) to obtain absolute receptor numbers as well as detailed spatial information of the synapse at the nanometer scale. We have further examined to what extent the molecular organization is maintained throughout adult development and during GlyRα1-deficiency. We show that GlyRs are packed at a constant density of about 2000 receptor complexes per $\mu m^2$ at mature synapses, suggesting that they are assembled in a stereotypic fashion. This GlyR molecular organization is

maintained in the hyperekplexia model *oscillator* despite a decrease in ventral synapse size, indicating that GlyRα1-deficiency does not affect the integrity of the synaptic arrangement as such. Collectively, these results provide the structural basis for understanding the mechanisms underlying receptor availability and integration of neurotransmitter-induced signals.

## Results

### Generation of a KI model expressing endogenous levels of mEos4b-GlyRβ

In order to quantify GlyR numbers and their precise distribution at native synapses we generated a knock-in (KI) mouse model expressing endogenous mEos4b-tagged GlyRβ subunits (Fig. S1). The β-subunit drives the synaptic localization of the receptor through direct interactions with the synaptic scaffold protein gephyrin at inhibitory synapses (Kim et al., 2006; Meyer et al., 1995). To date, labeling the β-subunit has proven difficult and has thus limited the study of the receptor. The coding sequence of mEos4b was inserted in exon 2 of the *Glrb* gene by homologous recombination supported by a guide RNA (CRISPR-Cas9) to increase recombination efficiency (ICS, Illkirch, France). The correct insertion was confirmed by amplification and sequencing of genomic DNA. Semi-quantitative RT-PCR revealed that equal concentrations of $Glrb^{Eos}$ and the wild-type transcript ($Glrb^{WT}$) are expressed in heterozygous animals. When bred to homozygosity, KI animals reach adulthood and display no overt phenotype, suggesting that the presence of the N-terminal fluorophore does not affect receptor expression and function.

### Quantitative confocal imaging of endogenous mEos4b-GlyRβ and mRFP-gephyrin at native spinal cord synapses

To verify the expression and synaptic targeting of the mEos4b-GlyRβ protein we carried out quantitative confocal imaging in 40 µm vibratome tissue sections. $Glrb^{Eos}$ animals were crossed with a KI mouse line expressing mRFP-tagged gephyrin to visualize inhibitory postsynaptic densities (PSDs) (Specht et al., 2013). Since the synaptic localization of the GlyR is strictly dependent on its interaction with gephyrin (Patrizio et al., 2017), we expected a high degree of co-localization of the two proteins in the brainstem and spinal cord (Zeilhofer et al., 2005). Indeed, mEos4b-GlyRβ was widely expressed at inhibitory synapses in the thalamus, midbrain, pons and medulla (Fig. S1). Very little fluorescence was detected in the forebrain, despite the high reported expression of the *Glrb* transcript (Fujita et al., 1991; Malosio et al., 1991; Weltzien et al., 2012).

In the spinal cord, we observed bright punctate mEos4b-GlyRβ signals throughout the gray matter, with the exception of the superficial laminae of the dorsal horn, where the intensity of the green fluorescence was markedly lower (Fig. 1A). The expression of mEos4b-GlyRβ and mRFP-gephyrin in homozygous and heterozygous animals was quantified in confocal images of thoracic and lumbar spinal cord slices at 2 months (Fig. 1B) and 10 months of age (Fig. S2). The integrated mEos4b intensity at gephyrin-positive ventral horn synapses was exactly two times higher in *Glrb*$^{Eos/Eos}$ mice than in *Glrb*$^{Eos/WT}$, demonstrating that both alleles are expressed with the same efficiency, and that the mEos4b fluorophore does not affect the synaptic localization of the receptor complexes. To confirm that the confocal image acquisition was in the linear dynamic range we bleached the mEos4b fluorophores by repeatedly scanning the same tissue area at constant laser power (Fig. 1A, white square), which resulted in a linear decay of pixel intensities over a range of more than 20 fold (Fig. 1C).

Across the spinal cord slices, the intensity of synaptic mEos4b-GlyRβ puncta increased from dorsal to ventral both in homozygous (Fig. 1D-E) and in heterozygous animals (Fig. S2). Similarly, mRFP-gephyrin fluorescence was higher and more variable in the ventral horn, suggesting that synapses were on average about twice as big as those in the dorsal horn, despite being fewer in number (Fig. 1F, S2). The mEos4/mRFP ratio was relatively equal across the spinal cord with the exception of the superficial layers of the dorsal horn, where gephyrin levels largely exceeded the GlyRs (Fig. 1A and D). The lower GlyR-scaffold occupancy of synapses in laminae I-III can be explained by the predominant expression of $GABA_A$Rs that compete for receptor binding sites at these mixed inhibitory synapses (Alvarez et al., 1996; Lorenzo et al., 2014; Todd et al., 1996).

**Dual-color super-resolution imaging of glycinergic spinal cord synapses**

To quantify the observed structural differences at super-resolution, we combined radial fluctuation (SRRF) analysis of mRFP-gephyrin and photo-activated localization microscopy (PALM, a form of SMLM) of mEos4b-GlyRβ in spinal cord tissue from double KI animals. Sucrose impregnated cryosections of 2 µm thickness were prepared from dorsal and ventral tissue and placed on gridded coverslips (Fig. 2A). SRRF and PALM images were acquired sequentially. First, mRFP signals were recorded with high intensity 561 nm laser illumination

until all mRFP fluorophores were bleached (10,000 frames). mEos4b was then photoconverted with increasing 405 nm laser intensity and imaged at 561 nm for 25,000 frames until all available fluorophores were exhausted. By acquiring both fluorophores in the same emission band (607/36 nm), any chromatic misalignment between the two super-resolved images was eliminated. SRRF reconstruction was carried out on the raw mRFP image sequence and PALM images were generated from individual mEos4b detections using Gaussian peak fitting (Fig. 2B).

The majority of synaptic clusters were small and spherical or elongated. Larger clusters displaying a variety of morphologies including elongated shapes seen in side-view (Fig. 2B) as well as convoluted structures which were more frequently seen in the ventral horn (Fig. S3). As expected of two directly interacting synaptic components the degree of co-localization of mEos4b-GlyRβ and mRFP-gephyrin was very high, with mean intensity correlation quotients (ICQ) around 0.3 (Fig. 2C and S3). Minor mismatches between the super-resolution images are explained by the fact that the majority of synapses are seen in cross-section and that the two fluorophores are located on opposite sides of the postsynaptic membrane (~30 nm distance, (Specht et al., 2013)). There were no obvious differences between the ICQ values of dorsal versus ventral synapses (0.28-0.3), indicating equivalent GlyRβ-gephyrin binding in the two regions. It should be noted that the ICQ reflects relative fluctuations between images and is not sensitive to absolute differences in signal intensities, resulting in similar ICQ values in animals that are heterozygous or homozygous for mRFP-gephyrin (Fig. 2C). Quantitative comparison of mEos4b-GlyRβ and mRFP-gephyrin intensities confirmed that the amounts of receptor and scaffold proteins are closely correlated, and that the occupancy of receptor binding sites is the same in the dorsal and ventral horn, independent of synapse size (Fig. 2D and S3). To estimate the sizes of the synapses we applied a density threshold to the PALM pointillist images and calculated the areas of the mEos4b-GlyRβ clusters (Fig. 2E). The mean synapse area in the ventral horn was larger and more variable than in the dorsal region, both in animals of 2 and 10 months of age (Fig. 2F). We also remarked that the overall number of synapses in ventral horn tissue was lower compared to the dorsal horn, significantly so by 10 months (Fig. 2G, see also Fig. 1F and S2). The inverse relationship between synapse number and size is likely due to the presence of different cell types in the two regions, specifically Renshaw cells and large motor neurons in the ventral horn that require strong inhibitory control (e.g. (Bhumbra et al., 2014)).

**Absolute quantification of GlyR numbers and densities at native spinal cord synapses**

Given that mEos4b-GlyRβ subunits are expressed at endogenous levels in *Glrb*$^{Eos/Eos}$ animals and that all the fluorophores were exhausted during the PALM recordings, we were able to count the absolute number of GlyR complexes at native spinal cord synapses. The total number of mEos4b-GlyRβ detections at synapses (Fig. S4) was converted into molecule numbers, taking into account the blinking properties of the fluorophore and the $\alpha_3$:$\beta_2$ stoichiometry of the pentameric GlyR complex (Durisic et al., 2014; Patrizio et al., 2017). To this aim, the average number of detections per fluorophore (detections/burst) and the fraction of functional fluorophores (probability of detection, $P_{det}$; Fig. S5) were determined in each set of experiments using extrasynaptic receptor complexes (Fig. 2E, red arrowheads). We calculated a median copy number of 114 pentameric GlyR complexes at dorsal horn synapses and twice that number at ventral horn synapses in 2 month old animals (Fig. 2H). Copy numbers were almost identical at 10 months (Fig. S6), indicating that the glycinergic network was mature at both time points. These numbers exceed estimates derived from electrophysiological recordings in new-born, juvenile and adult rat spinal cord neurons that suggest an activation ranging from 7 up to about 110 GlyRs during an average miniature inhibitory postsynaptic current (mIPSC) (Chery and de Koninck, 1999; Oleskevich et al., 1999; Singer and Berger, 1999; Takahashi, 1992). The high absolute numbers of GlyRs measured by fluorophore counting therefore imply that the available receptors are not saturated by quantal release, which is likely to increase the dynamic range of postsynaptic inhibition (Alvarez, 2017).

Our quantitative PALM data further demonstrate that differences in receptor numbers result from differences in synapse size (Fig. 2F). By combining the two parameters, we derived mean GlyR densities of ~2000 µm$^{-2}$ (Fig. 2I, S6). Similar receptor densities of 1250 µm$^{-2}$ and ~2000 µm$^{-2}$ have been measured at GABAergic synapses in cerebellar stellate cells and in cultured hippocampal neurons, respectively (Liu et al., 2020; Nusser et al., 1997). We saw no differences in the GlyR packing density at dorsal and ventral horn synapses, nor did we find a clear size dependence, as determined by linear regression of all synapses (Fig. 2I) and the evolution of the coefficient of variation of GlyR density with respect to synapse area (Fig. S6). These findings are significant because they indicate that GlyR density is constant and largely independent of neuron type, embryonic origin or physiological function. Assuming that

gephyrin molecules are clustered at densities of up to 9000 µm$^{-2}$ (Specht et al., 2013), our data also suggest that close to 50% of the receptor binding sites are occupied by GlyRs at native spinal cord synapses, in line with earlier observations of GlyR subunits that were overexpressed in cultured neurons (Patrizio et al., 2017).

**Quantitative SR-CLEM of GlyRβ molecular organization**

To integrate the results of molecule counting with three-dimensional ultra-structural information and the exact synapse size, we further analyzed dorsal and ventral horn synapses by SR-CLEM. Previously imaged cryosections of *Glrb*$^{Eos/Eos}$ tissue from 10 month old animals were embedded in epoxy resin, and ultra-thin (70 nm) serial sections were collected on EM slot grids with an ultramicrotome (Fig. 3A). After osmium tetroxide enhancement, electron micrographs of identified synapses were acquired in all serial sections and registered manually, using the coverslip grids and cellular structures as reference (Fig. 3B-C). All of the synapses that were both, imaged by PALM and reconstructed with EM were functionally mature, as judged by the apposition of a single presynaptic terminal containing synaptic vesicles. In line with our PALM data we found that glycinergic synapses in the ventral horn were substantially larger and more variable in size than those in the dorsal horn (Fig. 3C-D). There was good correspondence between the calculated synapse areas in the EM and PALM image reconstructions, even though PALM underestimated the sizes of some large ventral horn synapses (Fig. S7). This is probably due to the fact that a majority of synapses are tilted, and that the axial component of the area is not captured in the SMLM projections. Whereas most synapses in the dorsal horn were macular, ventral synapses were frequently composed of sub-domains (Fig. 3E-G). In agreement with earlier studies (Alvarez et al., 1997; Lushnikova et al., 2011; Santuy et al., 2018), the degree of complexity scales with the size of the PSD (Fig. 3F), and was taken into account for the calculation of the combined area in the EM serial sections.

The ratio of GlyR copy numbers and the area of the inhibitory PSDs obtained by EM resulted in average receptors densities of approximately 2000 µm$^{-2}$ (Fig. 3H). Consistent with our PALM estimates we did not observe significant differences between synapses in the dorsal and the ventral horn (Fig. 2I, S6). Furthermore, the GlyR packing density was not dependent on synapse size (Fig. 3I), supporting an earlier proposal (Lim et al., 1999). This suggests that GlyRs are assembled in a systematic manner, where receptor numbers increase linearly with synapse size. Since the morphological complexity of synapses increases with size, it can also

be concluded that GlyR occupancy at individual sub-domains of the PSD is uniform. GlyR densities were indeed not significantly different within sub-clusters of reconstructed synapses (Fig. 3G and I, black data points). Together, these findings point to a tight regulation of the architecture of glycinergic synapses across different molecular length scales, where GlyRs are arranged in sub-synaptic signaling units.

**Integrity of GlyR molecular arrangement is unaltered in the hyperekplexia mouse model *oscillator***

Having identified that GlyRs have a stereotypic molecular organization that is maintained throughout adulthood and across synapses in different neuronal circuits, we questioned whether this arrangement is altered in a mouse model of hyperekplexia, a motor-related neurological disease that significantly impacts motor processing in the ventral horn of the spinal cord. The mouse mutation *oscillator* (*Glra1*$^{spd\text{-}ot/spd\text{-}ot}$) is recessively inherited and causes a microdeletion and frameshift in the TM3-4 intracellular loop of the GlyRα1 subunit leading to subunit truncation and subsequent loss of functional GlyRs at synapses (Kling et al., 1997). Homozygous *oscillator* mice do not live past 3 weeks of age (Buckwalter et al., 1994). In contrast, heterozygous animals have a normal lifespan and exhibit a more subtle phenotype. *Glra1*$^{spd\text{-}ot/WT}$ mice display an increased startle reflex and lower GlyRα1 levels (Kling et al., 1997), making them a suitable model for human hyperekplexia. We generated mutant mice that were homozygous for mEos4b-GlyRβ (as described above) and heterozygous for *oscillator* (*Glrb*$^{Eos/Eos}$ / *Glra1*$^{spd\text{-}ot/WT}$) as well as wild-type littermates (*Glrb*$^{Eos/Eos}$ / *Glra1*$^{WT/WT}$). In these experiments, inhibitory synapses were detected by immunolabeling of endogenous gephyrin using mAb7a antibody.

Quantitative confocal imaging in 40 µm vibratome tissue sections showed bright punctate mEos4b-GlyRβ signals localized to synapses (Fig.4A). Across the spinal cord slices, the intensity of synaptic mEos4b-GlyRβ puncta increased from dorsal to ventral in homozygous WT animals (Fig. 4B), replicating the intensity profile observed previously (Fig. 1D). The intensity of synaptic mEos4b-GlyRβ puncta in *oscillator* animals were substantially lower than those of WT littermates, which explains the reductions in membrane levels of GlyR and gephyrin previously observed by Western blotting (Kling et al., 1997). The mEos4/gephyrin-7a ratio was relatively equal across the spinal cord with greater variation seen in *oscillator*. No ectopic GlyRβ clusters were detected, meaning that GlyRs and gephyrin always

colocalized (Fig. S8). The number of gephyrin-positive synapses across the spinal cord remained unchanged between WT and *oscillator*.

Using our quantitative PALM approach, we determined the number and size of glycinergic synapses in tissue slices of dorsal and ventral spinal cord, as well as the mEos4b detection density, in order to understand the alterations in glycinergic synapse architecture in this mutant mouse model. In WT animals we observed small and spherical dorsal synapses and larger, elongated ventral synapses, while *oscillator* synapses appeared small in both dorsal and ventral tissue. (Fig. 5A). This was confirmed by quantitative analysis. The mean synapse area in the ventral horn was significantly larger than in the dorsal region in WT animals (Fig. 5B), in agreement with our earlier data (Fig. 2F). However, this difference was lost in *Glra1*$^{spd\text{-}ot/WT}$ littermates. The overall number of synapses was lower in ventral horn tissue compared to the dorsal horn in both WT and *oscillator* animals (Fig. 5C). These data suggest that the decrease in functional receptors in heterozygous *oscillator* mice manifests itself as a reduction in the size of ventral synapses.

We further quantified the total number of mEos4b-GlyRβ detections at synapses (Fig.5D) and found that the number and distribution of WT mice detections matched that of 2 and 10 month old WT animals analyzed previously (Fig. S4). We found similar numbers of detections in *oscillator* dorsal synapses compared to WT littermates, however in ventral tissue we found a shift towards lower detection numbers per synapse, indicative of smaller synapses. By combining the measurements of synapse area with the number of detections per synapse we could derive the receptor density. Consistent with our previous PALM data, we found a constant density independent of synapse size in WT mice, as determined by the shallow slope of the linear regression (Fig.5E). We found a similar and constant GlyR packing density in synapses of *oscillator* mice. This suggests that despite a decrease in the total numbers of functional GlyRs in the heterozygous *oscillator* mouse model the molecular organization underlying receptor clustering within the synapse is maintained, in line with the lack of an overt neuromotor phenotype in these animals. In other words, the receptors are assembled stereotypically in the disease model, as in WT, with synapse size consistently scaling with receptor number. Together, our findings describe a highly regulated architecture of glycinergic synapses in both WT animals as well as in a model of synaptic pathology, providing a structural basis of glycinergic signaling.

## Discussion

Combining single molecule PALM imaging, molecular counting and 3D electron microscopy we have shown that glycinergic synapses in different regions of the spinal cord follow the same structural principle, insofar as their receptor-scaffold occupancy and packing densities are the same. This uniformity extends to the sub-synaptic level. The presence of so-called sub-synaptic domains (SSDs) at inhibitory synapses has been shown by super-resolution microscopy (Crosby et al., 2019; Dzyubenko et al., 2016; Pennacchietti et al., 2017; Specht et al., 2013). However, it remains controversial whether the identified patterns represent the overall structure of the PSD itself or whether they reflect intra-synaptic variations in molecule clustering. Our quantitative SR-CLEM data lend support to the first model, whereby inhibitory PSDs in the spinal cord are composed of sub-domains that shape the distribution of the GlyRs. This organization is achieved through direct interactions between GlyRs and gephyrin, as shown by the close correspondence between the receptors and scaffold proteins. As such, the GlyR sub-clusters at spinal cord synapses do not constitute SSDs within the PSD in the strict sense, since they exhibit uniform binding to the synaptic scaffold (discussed in (Yang and Specht, 2019)). The stereotypic GlyR density within SSDs observed in our study supports the idea that these structures can instead be equated with the convolutions of the synaptic junction observed by EM (Alvarez et al., 1997; Lushnikova et al., 2011; Peters and Palay, 1996; Santuy et al., 2018). The formation of these convolutions is probably a consequence of gephyrin oligomerization that appears to introduce an asymmetry in the synaptic scaffold. The situation may be different at GABAergic synapses, where the co-existence of gephyrin-dependent and gephyrin-independent clustering mechanisms could lead to the formation of spatially more restricted SSDs containing different $GABA_AR$ subtypes (Pennacchietti et al., 2017; Specht, 2020).

The nanoscale organization of inhibitory PSDs is the same in glycinergic neurons in the dorsal and the ventral spinal cord, despite their different embryonic origins. Ventral horn synapses are generally larger, more complex and contain more GlyRs, suggesting that the size of the synapse is differentially regulated in a regional and cell type specific manner to adjust the level of glycinergic inhibition. As such, these synapses may be particularly well adapted to motor circuits, assuring strong and reliable inhibition of the postsynaptic neuron (Alvarez, 2017). At the same time, the long and tortuous perimeter of the PSD is likely to accelerate the dynamic exchange of GlyRs and other synaptic components (Chow et al., 2017; Santuy et al., 2018), thereby promoting the molecular plasticity at complex inhibitory synapses (Specht,

2020). It can further be argued that large and morphologically complex synapses may be particularly well adapted to integrate fast temporal, or indeed multi-vesicular release arising from one or more presynaptic sites, thus providing a strong and reliable inhibition of the postsynaptic neuron while maintaining fast neurotransmitter clearance (discussed in (Alvarez, 2017; Rudolph et al., 2015)).

In addition, our data show that GlyR density and occupancy do not change between 2 and 10 months of age, indicating that receptor clustering is fully mature by the earlier time point. Studies of normal aging of spinal cord synapses are scarce, and its effect on receptor organization has not been studied. Broadhead and colleagues (Broadhead et al., 2020) report no difference between the number of excitatory synapses in the ventral horn and only a slight increase in dorsal synapses between 2 to 9 month old mice. Broadly in line with these findings, we found no difference in the number of synapses, synapse area, and GlyR packing density in dorsal and ventral tissue between 2 and 10 months. Thus, glycinergic PSDs show considerable control over their molecular composition throughout adulthood, further emphasizing the functional significance of their synaptic architecture in both sensory and motor signaling. Our data therefore suggest that a constant GlyR density potentially provides the most efficient organization of the glycinergic PSD, while enabling the refinement of the size and complexity of the synapse due to ongoing neural activity.

The neuromotor disease hyperekplexia results from defects in glycinergic inhibition in humans. Several mouse models with analogous mutations in the *Glra1* gene recapitulate the phenotype of exaggerated startle reflexes and muscle stiffness (Schaefer et al., 2018). In general, the mutations in the various mouse models are less well tolerated than in humans, often with lethal phenotypes in homozygotes. Hyperekplexia can be recessively or dominantly inherited in humans, but neither has been shown to cause lethality. The *oscillator* model, whilst lethal as a homozygous, displays a relatively mild phenotype in heterozygous animals, with a measurable startle reflex and normal lifespan (Kling et al., 1997). Heterozygous *oscillator* therefore represents a relevant model for the subtler phenotype in humans and the long-term stability of glycinergic synapses beyond the developmental stage at which lethality occurs in homozygous animals. However, it is not known how the reduced GlyR levels in the $Glra1^{spd\text{-}ot/WT}$ hypomorph can affect (and sustain) functional motor networks. We characterized the molecular organization of heterozygous *oscillator* synapses and show that GlyR packing follows the same principle as in WT synapses, even though the total number of

available functional receptors is reduced, resulting in smaller synapses in the ventral spinal cord. This further emphasizes that the stereotypic arrangement of GlyRs dictates the size of the PSD. Most of the synapses that are formed in heterozygous *oscillator* likely achieve a size threshold capable of sustaining glycinergic signaling without serious motor defects. The lack of fundamental structural changes at glycinergic synapses further suggests that no or only limited compensatory effects take place in *oscillator*, in agreement with earlier findings that α1β GlyR complexes cannot be compensated for by other subunit configurations, α1-homopentamers or $GABA_A$Rs (Schaefer et al., 2012). Our findings thus provide a new perspective into the molecular basis of GlyRα1-deficiency in an animal model of human hyperekplexia.

Taken together, our data show that dorsal and ventral synapses are distinct populations. Ventral horn synapses have much higher GlyR copy numbers, even though receptor density is not different. In contrast to the relatively compact, macular synapses in the dorsal horn, ventral horn synapses achieve a greater receptor number by enlarging the synaptic surface, thus multiplying the sites of signal transmission. These region-specific glycinergic synapse morphologies are likely to underlie functional differences at sensory (dorsal) versus motor (ventral) circuits.

**Acknowledgements**

SAM is supported by a Fondation pour la Recherche Médicale (FRM) postdoctoral fellowship (SPF201809007132). NS was supported by funds of the Bavarian State Ministry of Science and the Arts and the University of Würzburg to the Graduate School of Life Sciences (GSLS), University of Würzburg. Research in our laboratory at IBENS is funded by the European Research Council (ERC, Plastinhib), Agence Nationale de la Recherche (ANR, Synaptune and Syntrack), Labex (Memolife) and France-BioImaging (FBI). CV is supported by the Deutsche Forschungsgemeinschaft (DFG, VI586). We acknowledge the use of the EM platform of IBENS. We thank Pascal Legendre (ENP, Inserm) for insightful discussions and Constant Morez and Nadine Schibille for helpful comments on the manuscript. We also thank Marie-Christine Birling and Eve Geronimus from the Institut Clinique de la Souris (ICS, Illkirch, France) for the generation of the C57BL/6N-*Glrb*$^{tm1Ics}$ mouse line.

## Author contributions

SAM and CGS planned the experiments; SAM, PR, OG, AC, AD, NS and CGS performed the experiments; SAM, PR and CGS analyzed the data; CV generated the oscillator strain; AT secured funding; SAM and CGS wrote the manuscript; all authors read and approved the manuscript.

## Declaration of interests

The authors declare no competing interests.

## Data and materials availability

All data are available upon request.

## Materials and Methods

### KI mouse model generation

The knock-in (KI) mouse line C57BL/6N-*Glrb*$^{tm1Ics}$ (MGI:6331106) carrying the mutant allele *Glrb*$^{tm1(Eos4)Ics}$ (MGI:6331065) was created by homologous recombination at the Institut Clinique de la Souris (ICS, Illkirch, France). Flanked by 5' and 3' homology arms of 1.23 kb and 3.49 kb, respectively, the targeting vector encompassed exon 2 of the *Glrb* gene with an insertion of the coding sequence of mEos4b, as well as a *floxed* neomycin selection cassette containing the Cre recombinase under control of protamine promoter in intron 2-3. The selection cassette was excised in the F1 generation by germline expression of Cre, resulting in a single *loxP* site in intron 2-3 of the *Glrb* locus (Fig. S1A). The correct insertion of the mEos4b coding sequence was confirmed by sequencing of genomic *Glrb*$^{Eos/Eos}$ tail DNA. Genotyping was done using three primers (primer 1: TACCTTCTTGTTTTCTCTCC; primer 2: GTCTGTTTTCCCTCATAAGG; primer 3: TCGCTTTTGTAAATGATATGG) for the amplification of the mutant *Glrb*$^{Eos}$ (243 bp product) and/or the wild-type alleles (404 bp).

Purified spinal cord mRNA of *Glrb*$^{Eos/Eos}$, *Glrb*$^{Eos/WT}$ and *Glrb*$^{WT/WT}$ animals was reverse transcribed (primer 6: GGAGTCTAACAGTAATCTGG), and amplified (primer 4: AGGCGCGTCAAACTCGG; primer 5: CCATACCAACCAATGAAAGG). The correct splicing of the mutant transcript was confirmed by sequencing of amplified cDNA. For semi-quantitative RT-PCR, the *Glrb*$^{Eos/Eos}$ mRNA was spiked with wild-type cDNA at a ratio of 1:2, 1:1 and 2:1 and amplified (Fig. S1B).

All experiments (with the exception of the data in Fig. S1A-B, 4, 5 and S8) were carried out with F2 animals resulting from a cross between the KI line C57BL/6N-*Glrb*$^{tm1Ics}$ (see above) and a KI mouse line expressing mRFP-tagged gephyrin (Machado et al., 2011) in the C57BL/6J strain, meaning that the mice had a mixed C57BL/6N x C57BL/6J genetic background.

Adult *Glra1*$^{spd\text{-}ot}$ mice (*oscillator*, JAX stock #000536) from Jackson Laboratories (Bar Harbor, ME, USA) were transferred to the animal facility of the Institute of Clinical Neurobiology (Würzburg, Germany). Genotyping was done using primer 7: GCCTCCGTGCTTTCTCCCTGC and primer 8: CCAGCCACGCCCCAAAG for the amplification of the mutant *Glra1*$^{spt\text{-}ot}$ (187 bp product) and/or the wild-type alleles (194 bp). *Oscillator* mice were backcrossed into the C57BL/6J background for at least 15 generations. Heterozygous *Glrb*$^{Eos/WT}$ animals were crossed with heterozygous *oscillator* mice for two generations giving rise to F2 heterozygous *oscillator* animals that are homozygous for the *Glrb*$^{tm1(Eos4)Ics}$ allele (*Glra*1$^{+/spd\text{-}ot}$/*Glrb*$^{Eos/Eos}$). These animals had a mixed C57BL/6N x C57BL/6J genetic background and were used for the experiments shown in Fig. 4, 5 and S8.

All experiments were in accordance with European Union guidelines and approved by the local veterinary authorities. Animals at IBENS were treated in accordance with the guidelines of the French Ministry of Agriculture and Direction Départementale des Services Vétérinaires de Paris (École Normale Supérieure, Animalerie des Rongeurs, license B 75-05-20). Procedures carried out at the Institute for Clinical Neurobiology were approved by the Veterinäramt der Stadt Würzburg and the Committee on the Ethics of Animal Experiments (Regierung von Unterfranken, Würzburg) and authorized under reference numbers 55.2-2531.01-09/14; 55.2.2-2532.2-949-31.

**Spinal cord and brain tissue preparation and vibratome slices**

Mice were sacrificed at 2 and 10 months of age by perfusion with 4% w/v paraformaldehyde (PFA; Polysciences, EM grade) and 0.1% v/v glutaraldehyde (GA; Clinisciences) in phosphate buffered saline (PBS, pH 7.4). Perfused animals were kept on ice for 30 min, followed by the dissection of the brain and spinal cord in PBS. Tissue was post-fixed in 4% w/v PFA in PBS overnight at 4 °C. Brain and spinal cord tissue was rinsed in PBS, cut into smaller segments of thoracic and lumbar regions of the spinal cord and sliced on a vibratome

(Leica) at a thickness of 40 µm (for confocal imaging) and 300 µm (for Tokuyasu preparation), and stored in PBS at 4 °C.

**Confocal imaging and analysis**

In order to label the gephyrin in the oscillator and WT littermates, free-floating vibratome slices (40 µm thickness) were blocked and permeabilized in PBS containing 0.25% Triton X100 (Sigma) and 0.1% fish gelatin (Sigma) for 1 h, and immunolabeled with a primary antibody against gephyrin (mouse, mAb7a, 1:500 dilution, Synaptic Systems, #147011) in PBS containing 0.1% Triton X100 and 0.1% fish gelatin overnight, followed by 3 hour incubation with a Cy3-conjugated secondary antibody (goat anti mouse,1:1000, Invitrogen).

Glass slides (Vector Laboratories) were cleaned with 70% v/v ethanol (Sigma) and vibratome sections were rinsed 3 times in PBS and mounted onto the glass slides. The glass slides were then briefly rinsed in distilled water and dried. A drop of VectaShield (Vector Laboratories) was added to each spinal cord section and covered with a #1.5 glass coverslip, which was sealed with PicoDent Twinsil Speed (equal weights of catalyst and base). Slides were stored at 4 °C for confocal imaging.

Confocal imaging was carried out on a Leica SP8 TCX microscope using a Leica HC PL APO 40x/1.30 NA oil-immersion objective (Leica) and captured in 8-Bit using the Leica LAS-X software with setting HyD3. Images were captured sequentially, with laser illumination at wavelength 570 nm (mRFP, Cy3) imaged first, followed by laser illumination at 491 nm wavelength (mEos4). A cross-section from the dorsal horn to the ventral horn was imaged at a zoom of 5, speed of 25, 512 x 512 pixel (px) format. For decay analysis, 8 consecutive frames were captured at a zoom of 5, speed 25, 512 x 512 px format. To tile the whole spinal cord, images were captured in at a zoom of 1, speed 100, 256 x 256 px format.

To ensure alignment of the clusters for the decay traces, images were opened in the image analysis software ICY, and the rigid registration plug-in used, taking the first frame of mRFP-gephyrin as reference. The mRFP-gephyrin/ and mEos4b-GlyRβ channels were then separated and the Spot Detector plug-in (de Chaumont et al., 2012) used to identify the clusters in each frame in the mRFP-gephyrin channel, with the identified clusters saved as a region of interest (ROI) set. Using the image analysis software FIJI, the identified mRFP-gephyrin positive cluster ROI-Set was used to identify inhibitory synapses in the first frame of

the mEos4b-GlyRβ channel. These inhibitory synapses were binned based on mEos4b intensity gray levels (5-12, 13-24, 25-49, 50-74, 75-99, 100-124, 125-255) in frame 1 and a new ROI-Set generated for each bin. Using the frame 1 intensity ROI-Sets, the integrated intensity of mEos4b was then measured at individual clusters across the 8 frames. This enabled decay analysis of mEos4b intensity at synapses relative to their starting intensity, see Fig. 1C.

In order to analyze the intensity of mRFP-gephyrin and mEos4b-GlyRβ clusters within the spinal cords from mice of different genotypes, the identified mRFP-gephyrin clusters from the first frame of the decay traces (as measured by the ICY Spot Detector plug-in, see above) were used to measure the relative intensity of mRFP-gephyrin and mEos4b-GlyRβ clusters at those locations. The ROI-Set of all mRFP-gephyrin positive clusters was used in FIJI to identify inhibitory synapses, where the integrated intensity of mRFP and mEos4b was measured for each synapse (Fig. 1B).

For the cross-sectional analysis, the mRFP-gephyrin/gephyrin-7a clusters were identified across the imaged tissue using the ICY Spot Detector plug-in, as described above, and saved as an ROI-Set. In FIJI the integrated intensity of these identified clusters was measured in the mRFP-gephyrin/gephyrin-7a channel and the mEos4b-GlyRβ channel (Fig. 1D and 1F).

**Cryosectioning of sucrose impregnated spinal cord tissue**

Sucrose impregnated cryosections were prepared using a ultracryotomy protocol adapted from (Tokuyasu, 1973). The 300 µm spinal cord vibratome slices were transferred into a 2.3 M sucrose solution in PBS overnight at 4°C and micro-dissected to isolate gray matter of the dorsal and the ventral horn region. These fragments were placed individually on top of drops of sucrose solution on aluminium EM pins (Leica) and immediately frozen in liquid nitrogen. Sections of 2 µm thickness were sliced on an ultramicrotome (Leica EM UC6) at -80°C and placed onto gridded coverslips (type 1.5 H, Ibidi GmbH), covered in PBS, and stored at 4°C for a maximum of 5 days before imaging.

**Single molecule localization microscopy (SMLM)**

Sucrose cryosections on gridded coverslips were rinsed once in PBS, and imaged in PBS. Dual-colour super resolution images were acquired on an inverted Nikon Eclipse Ti microscope with a 100x/1.49 NA oil-immersion objective, with an additional 1.5x lens in the

emission path, using an Andor iXon EMCCD camera (16-Bit, 107 nm pixel size), and NIS-Elements software (Nikon). An emission filter 607/36 was chosen for imaging both mRFP-gephyrin and mEos4b-GlyRβ. Brightfield images were taken of the whole grid square identifying tissue structures. Lamp images were taken of the unconverted mEos4b-GlyRβ and mRFP-gephyrin (10 frames of 100 ms, ND8). mRFP-gephyrin movies of 10,000 frames were recorded with HiLo 561 nm continuous laser illumination (output power 50% 400 mW, 50 ms frames). This was followed by 2 min of 100% 561 nm laser illumination to ensure all mRFP-gephryin was bleached. Movies of 25,000 frames were recorded with photoconversion of mEos4b-GlyRβ by 0.5 ms pulsed 405 nm laser illumination (gradually increased to 100% by frame 22,000) with continuous 561 nm laser illumination (output power 50% 400 mW, 50 ms frames). The focal plane was maintained using a Nikon perfect focus system.

**SMLM image analysis (SRRF and PALM)**

Frames 100-6000 of the mRFP-gephyrin movies were taken for analysis (to remove saturated frames at the beginning and bleached frames at the end) and were drift corrected and reconstructed using SRRF plugin for FIJI (Gustafsson et al., 2016).
Quantification of mEos4b-GlyRβ was carried out using a lab script for MATLAB (Mathworks). The mEos4b single fluorophores were detected by Gaussian fitting. The resulting pointillist images were drift corrected in the x/y plane using 5 dense clusters of detections over a sliding window of 2000 frames. Rendered images were produced with a pixel size of 10 nm, sigma 0.01.

The mRFP-gephyrin and mEos4b-GlyRβ rendered images were aligned by rigid registration using the FIJI plug-in TurboReg. The co-localization of mRFP-gephyrin and mEos4b-GlyRβ was carried out by individually cropping each synapse as separate images. The FIJI plug-in Intensity correlation quotient (ICQ) was then applied to each synapse (Li et al., 2004). The occupancy analysis was analyzed by thresholding the synapses in the mEos4b-GlyRβ images and measuring the intensity of each synapse in both channels. To analyse the PALM mEos4b-GlyRβ clusters, a lab written script for MATLAB (CountMol; (Patrizio et al., 2017)) was used to identify synapses (minimum number of detections 250, minimum cluster size 200 nm, maximum cluster size 3000 nm) and an intensity threshold of 0.1. For molecule conversion, CountMol was used to identify extrasynaptic receptor complexes (minimum number of detections 5, minimum cluster size 10 nm, maximum cluster size 120 nm). The number of detections per burst (identified as a minimum of 2 detections, with 1 burst per 1000 frames)

and the probability of detection $P_{det} = (1 - \frac{N_1/N_2}{2+N_1/N_2})$ were calculated, and used to convert the detections to mEos4b-GlyRβ molecules (Durisic et al., 2014; Patrizio et al., 2017).

**Electron microscopy (EM)**

Cryosections used for SMLM imaging on gridded coverslips were postfixed by incubation in 1% osmium tetroxide for 1 h at 4 °C, dehydrated in graded ethanol concentrations, and embedded in araldite epoxy resin. Grid squares imaged in SMLM were identified using the grid pattern imprinted in the resin. Serial ultra-thin 70 nm sections of these regions were cut, transferred onto formvar-coated EM grids (0.432 mm slot grids) using a UC6 ultramicrotome (Leica). Sections were counterstained with 5% uranyl acetate in 70% methanol for 10 min, then washed in distilled water and air dried before observation on a Philips TECNAI 12 microscope (Thermo Fisher Scientific).

For 3D synapse reconstruction, synapses were manually outlined in each serial section image using FIJI, followed by manual rotation and coarse alignment using the software GIMP, then fine alignment of the synaptic area with the Microscopy Image Browser (MIB) software. The aligned images were then opened in IMOD software to generate the 3D reconstruction.

The length of the PSD of identified synapses was measured in high magnification EM images with ImageJ software. The total PSD area was calculated as the cumulative length of the PSD in the entire stack of serial sections multiplied by the thickness of each section (70 nm). The segmentation index is the number of gaps in the PSD that were detected in the x/y plane of the images or along the z-axis (i.e. an interruption of the PSD in one or several continuous sections in the stack), and represents an estimate of the morphological complexity of the synapse.

**Graphing and statistical analysis**

All graphing and statistical analysis was carried out using the software GraphPad Prism v.8. Data were tested for normality of distribution using D'Agostino-Pearson and Kolmogorov-Smirnov tests. Data is represented as dot plots with median ± interquartile range (IQR), or histograms, unless otherwise stated. *$p < 0.05$, ** $p < 0.01$, *** $p < 0.001$, ns = not significant.

## References

Alvarez, F.J. (2017). Gephyrin and the regulation of synaptic strength and dynamics at glycinergic inhibitory synapses. Brain Res Bull *129*, 50-65.

Alvarez, F.J., Dewey, D.E., Harrington, D.A., and Fyffe, R.E. (1997). Cell-type specific organization of glycine receptor clusters in the mammalian spinal cord. J Comp Neurol *379*, 150-170.

Alvarez, F.J., Taylor-Blake, B., Fyffe, R.E., De Blas, A.L., and Light, A.R. (1996). Distribution of immunoreactivity for the beta 2 and beta 3 subunits of the GABAA receptor in the mammalian spinal cord. J Comp Neurol *365*, 392-412.

Bhumbra, G.S., Bannatyne, B.A., Watanabe, M., Todd, A.J., Maxwell, D.J., and Beato, M. (2014). The recurrent case for the Renshaw cell. J Neurosci *34*, 12919-12932.

Broadhead, M.J., Bonthron, C., Arcinas, L., Bez, S., Zhu, F., Goff, F., Nylk, J., Dholakia, K., Gunn-Moore, F., Grant, S.G.N., *et al.* (2020). Nanostructural Diversity of Synapses in the Mammalian Spinal Cord. Sci Rep *10*, 8189.

Buckwalter, M.S., Cook, S.A., Davisson, M.T., White, W.F., and Camper, S.A. (1994). A frameshift mutation in the mouse alpha 1 glycine receptor gene (Glra1) results in progressive neurological symptoms and juvenile death. Hum Mol Genet *3*, 2025-2030.

Chery, N., and de Koninck, Y. (1999). Junctional versus extrajunctional glycine and GABA(A) receptor-mediated IPSCs in identified lamina I neurons of the adult rat spinal cord. J Neurosci *19*, 7342-7355.

Chow, D.M., Zuchowski, K.A., and Fetcho, J.R. (2017). In vivo measurement of glycine receptor turnover and synaptic size reveals differences between functional classes of motoneurons in zebrafish. Curr Biol *27*, 1173-1183.

Chung, S.K., Bode, A., Cushion, T.D., Thomas, R.H., Hunt, C., Wood, S.E., Pickrell, W.O., Drew, C.J., Yamashita, S., Shiang, R., *et al.* (2013). GLRB is the third major gene of effect in hyperekplexia. Hum Mol Genet *22*, 927-940.

Chung, S.K., Vanbellinghen, J.F., Mullins, J.G., Robinson, A., Hantke, J., Hammond, C.L., Gilbert, D.F., Freilinger, M., Ryan, M., Kruer, M.C., *et al.* (2010). Pathophysiological mechanisms of dominant and recessive GLRA1 mutations in hyperekplexia. J Neurosci *30*, 9612-9620.

Crosby, K.C., Gookin, S.E., Garcia, J.D., Hahm, K.M., Dell'Acqua, M.L., and Smith, K.R. (2019). Nanoscale subsynaptic domains underlie the organization of the inhibitory synapse. Cell Rep *26*, 3284-3297 e3283.

de Chaumont, F., Dallongeville, S., Chenouard, N., Herve, N., Pop, S., Provoost, T., Meas-Yedid, V., Pankajakshan, P., Lecomte, T., Le Montagner, Y., *et al.* (2012). Icy: an open bioimage informatics platform for extended reproducible research. Nat Methods *9*, 690-696.

Durisic, N., Laparra-Cuervo, L., Sandoval-Alvarez, A., Borbely, J.S., and Lakadamyali, M. (2014). Single-molecule evaluation of fluorescent protein photoactivation efficiency using an in vivo nanotemplate. Nat Methods *11*, 156-162.

Dzyubenko, E., Rozenberg, A., Hermann, D.M., and Faissner, A. (2016). Colocalization of synapse marker proteins evaluated by STED-microscopy reveals patterns of neuronal synapse distribution in vitro. J Neurosci Methods *273*, 149-159.

Fujita, M., Sato, K., Sato, M., Inoue, T., Kozuka, T., and Tohyama, M. (1991). Regional distribution of the cells expressing glycine receptor beta subunit mRNA in the rat brain. Brain Res *560*, 23-37.

Gustafsson, N., Culley, S., Ashdown, G., Owen, D.M., Pereira, P.M., and Henriques, R. (2016). Fast live-cell conventional fluorophore nanoscopy with ImageJ through super-resolution radial fluctuations. Nat Commun *7*, 12471.

Haas, K.T., Compans, B., Letellier, M., Bartol, T.M., Grillo-Bosch, D., Sejnowski, T.J., Sainlos, M., Choquet, D., Thoumine, O., and Hosy, E. (2018). Pre-post synaptic alignment through neuroligin-1 tunes synaptic transmission efficiency. Elife *7*.

Harvey, R.J., Depner, U.B., Wassle, H., Ahmadi, S., Heindl, C., Reinold, H., Smart, T.G., Harvey, K., Schutz, B., Abo-Salem, O.M., *et al.* (2004). GlyR alpha3: an essential target for spinal PGE2-mediated inflammatory pain sensitization. Science *304*, 884-887.

Kim, E.Y., Schrader, N., Smolinsky, B., Bedet, C., Vannier, C., Schwarz, G., and Schindelin, H. (2006). Deciphering the structural framework of glycine receptor anchoring by gephyrin. Embo J *25*, 1385-1395.

Kling, C., Koch, M., Saul, B., and Becker, C.M. (1997). The frameshift mutation oscillator (Glra1(spd-ot)) produces a complete loss of glycine receptor alpha1-polypeptide in mouse central nervous system. Neuroscience *78*, 411-417.

Li, Q., Lau, A., Morris, T.J., Guo, L., Fordyce, C.B., and Stanley, E.F. (2004). A syntaxin 1, Galpha(o), and N-type calcium channel complex at a presynaptic nerve terminal: analysis by quantitative immunocolocalization. J Neurosci *24*, 4070-4081.

Lim, R., Alvarez, F.J., and Walmsley, B. (1999). Quantal size is correlated with receptor cluster area at glycinergic synapses in the rat brainstem. J Physiol *516 ( Pt 2)*, 505-512.

Liu, Y.T., Tao, C.L., Zhang, X., Xia, W., Shi, D.Q., Qi, L., Xu, C., Sun, R., Li, X.W., Lau, P.M., *et al.* (2020). Mesophasic organization of GABA(A) receptors in hippocampal inhibitory synapses. Nat Neurosci.

Lorenzo, L.E., Godin, A.G., Wang, F., St-Louis, M., Carbonetto, S., Wiseman, P.W., Ribeiro-da-Silva, A., and De Koninck, Y. (2014). Gephyrin clusters are absent from small diameter primary afferent terminals despite the presence of GABA(A) receptors. J Neurosci *34*, 8300-8317.

Lu, D.C., Niu, T., and Alaynick, W.A. (2015). Molecular and cellular development of spinal cord locomotor circuitry. Front Mol Neurosci *8*, 25.

Lushnikova, I., Skibo, G., Muller, D., and Nikonenko, I. (2011). Excitatory synaptic activity is associated with a rapid structural plasticity of inhibitory synapses on hippocampal CA1 pyramidal cells. Neuropharmacology *60*, 757-764.

MacGillavry, Harold D., Song, Y., Raghavachari, S., and Blanpied, Thomas A. (2013). Nanoscale Scaffolding Domains within the Postsynaptic Density Concentrate Synaptic AMPA Receptors. Neuron *78*, 615-622.

Machado, P., Rostaing, P., Guigonis, J.M., Renner, M., Dumoulin, A., Samson, M., Vannier, C., and Triller, A. (2011). Heat shock cognate protein 70 regulates gephyrin clustering. J Neurosci *31*, 3-14.

Malosio, M.L., Marquèze-Pouey, B., Kuhse, J., and Betz, H. (1991). Widespread expression of glycine receptor subunit mRNAs in the adult and developing rat brain. Embo j *10*, 2401-2409.

Maric, H.M., Mukherjee, J., Tretter, V., Moss, S.J., and Schindelin, H. (2011). Gephyrin-mediated gamma-aminobutyric acid type A and glycine receptor clustering relies on a common binding site. J Biol Chem *286*, 42105-42114.

Meyer, G., Kirsch, J., Betz, H., and Langosch, D. (1995). Identification of a gephyrin binding motif on the glycine receptor beta subunit. Neuron *15*, 563-572.

Nusser, Z., Cull-Candy, S., and Farrant, M. (1997). Differences in synaptic GABA(A) receptor number underlie variation in GABA mini amplitude. Neuron *19*, 697-709.

Oleskevich, S., Alvarez, F.J., and Walmsley, B. (1999). Glycinergic miniature synaptic currents and receptor cluster sizes differ between spinal cord interneurons. J Neurophysiol *82*, 312-319.

Patrizio, A., Renner, M., Pizzarelli, R., Triller, A., and Specht, C.G. (2017). Alpha subunit-dependent glycine receptor clustering and regulation of synaptic receptor numbers. Sci Rep *7*, 10899.

Pennacchietti, F., Vascon, S., Nieus, T., Rosillo, C., Das, S., Tyagarajan, S.K., Diaspro, A., Del Bue, A., Petrini, E.M., Barberis, A., *et al.* (2017). Nanoscale molecular reorganization of the inhibitory postsynaptic density is a determinant of GABAergic synaptic potentiation. J Neurosci *37*, 1747-1756.

Peters, A., and Palay, S.L. (1996). The morphology of synapses. J Neurocytol *25*, 687-700.

Rudolph, S., Tsai, M.C., von Gersdorff, H., and Wadiche, J.I. (2015). The ubiquitous nature of multivesicular release. Trends Neurosci *38*, 428-438.

Santuy, A., Rodriguez, J.R., DeFelipe, J., and Merchan-Perez, A. (2018). Study of the size and shape of synapses in the juvenile rat somatosensory cortex with 3D electron microscopy. eNeuro *5*.

Schaefer, N., Langlhofer, G., Kluck, C.J., and Villmann, C. (2013). Glycine receptor mouse mutants: model systems for human hyperekplexia. Br J Pharmacol *170*, 933-952.

Schaefer, N., Roemer, V., Janzen, D., and Villmann, C. (2018). Impaired glycine receptor trafficking in neurological diseases. Front Mol Neurosci *11*, 291.

Schaefer, N., Vogel, N., and Villmann, C. (2012). Glycine receptor mutants of the mouse: what are possible routes of inhibitory compensation? Front Mol Neurosci *5*, 98.

Singer, J.H., and Berger, A.J. (1999). Contribution of single-channel properties to the time course and amplitude variance of quantal glycine currents recorded in rat motoneurons. J Neurophysiol *81*, 1608-1616.

Specht, C.G. (2020). Fractional occupancy of synaptic binding sites and the molecular plasticity of inhibitory synapses. Neuropharmacology *169*, 107493.

Specht, C.G., Izeddin, I., Rodriguez, P.C., El Beheiry, M., Rostaing, P., Darzacq, X., Dahan, M., and Triller, A. (2013). Quantitative nanoscopy of inhibitory synapses: counting gephyrin molecules and receptor binding sites. Neuron *79*, 308-321.

Takahashi, T. (1992). The minimal inhibitory synaptic currents evoked in neonatal rat motoneurones. J Physiol *450*, 593-611.

Tang, A.H., Chen, H., Li, T.P., Metzbower, S.R., MacGillavry, H.D., and Blanpied, T.A. (2016). A trans-synaptic nanocolumn aligns neurotransmitter release to receptors. Nature *536*, 210-214.

Todd, A.J., Watt, C., Spike, R.C., and Sieghart, W. (1996). Colocalization of GABA, glycine, and their receptors at synapses in the rat spinal cord. J Neurosci *16*, 974-982.

Tokuyasu, K.T. (1973). A technique for ultracryotomy of cell suspensions and tissues. J Cell Biol *57*, 551-565.

Weltzien, F., Puller, C., O'Sullivan, G.A., Paarmann, I., and Betz, H. (2012). Distribution of the glycine receptor beta-subunit in the mouse CNS as revealed by a novel monoclonal antibody. J Comp Neurol *520*, 3962-3981.

Yang, X., and Specht, C.G. (2019). Subsynaptic domains in super-resolution microscopy: The treachery of images. Front Mol Neurosci *12*, 161.

Zeilhofer, H.U., Studler, B., Arabadzisz, D., Schweizer, C., Ahmadi, S., Layh, B., Bosl, M.R., and Fritschy, J.M. (2005). Glycinergic neurons expressing enhanced green fluorescent protein in bacterial artificial chromosome transgenic mice. J Comp Neurol *482*, 123-141.

## Figures and Legends

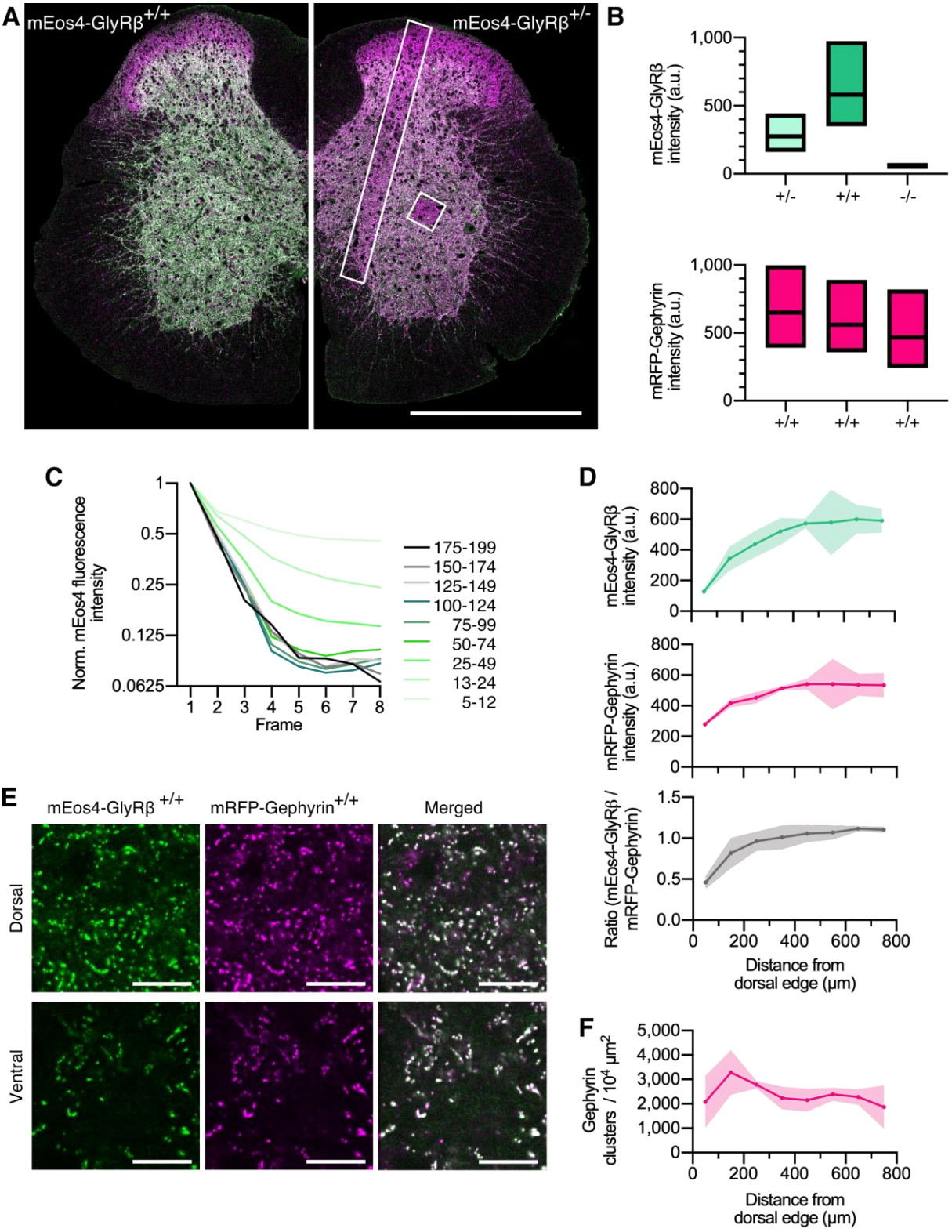


**Fig. 1. Quantitative confocal imaging.** (A) Representative confocal images of 40 μm spinal cord tissue sections from homozygous (+/+) and heterozygous (+/-) mEos4b-GlyRβ mice (green). Both mice are homozygous for mRFP-gephyrin (magenta). Scale bar = 0.5 mm. (B) Quantification of mEos4b-GlyRβ and mRFP-gephyrin fluorescent intensity of homozygous and heterozygous 2 month old animals. Plots show median and quartiles. N = 5 images per

786 condition. (C) Normalized fluorescent decay traces of homozygous mEos4b measured in the
787 area indicated by the white square in (A) over 8 consecutive frames. Intensities were binned
788 in the first image and tracked on an individual synapse basis across the 8 frames. (D) Mean
789 intensity ± 95% confidence interval of mEos4b-GlyRβ and mRFP-gephyrin measured from
790 distal edge of spinal cord in 2 month old homozygous mice. Intensities measured in region as
791 indicated by white rectangle in (A). N = 3 images. (E) Representative images of homozygous
792 mEos4b-GlyRβ and mRFP-gephyrin at dorsal and ventral synapses. Scale bar = 10 μm. (F)
793 Quantification of numbers of gephyrin clusters across the spinal cord. Plot shows mean ±
794 95% confidence interval. N = 3 images.
795

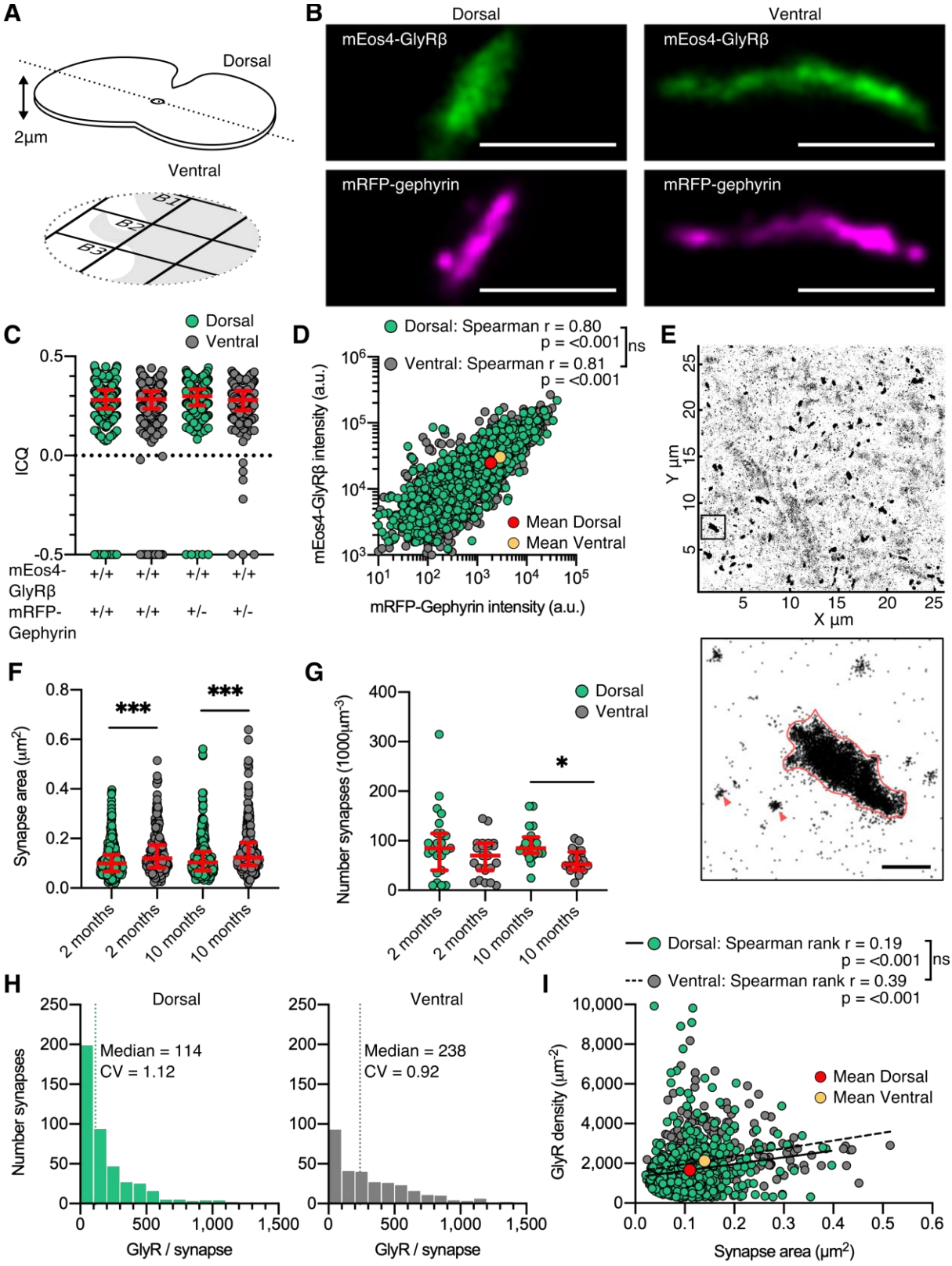


**Fig. 2. Dual-color super-resolution imaging.** (A) 2 µm cryosections of spinal cord tissue were cut from dorsal and ventral tissue and placed on gridded glass coverslips. (B) Representative SMLM reconstruction of mEos4b-GlyRβ and SRRF reconstruction of mRFP-gephyrin at single dorsal and ventral synapses. Scale bar = 500 nm. (C) Intensity correlation quotient (ICQ) of mEos4b-GlyRβ and mRFP-gephyrin in heterozygous and homozygous 2

month old mice. N = 357-604 synapses from 22 dorsal and 22 ventral images. (D) Quantification of GlyR-gephyrin occupancy. Non-parametric Spearman's rank shows the same positive correlation at dorsal and ventral synapses. (E) Pointillist reconstruction of mEos4b-GlyRβ detections. Insert shows a single synapse; red arrows indicate extrasynaptic receptor complexes. Scale bar = 500 nm. (F) Area of dorsal vs ventral synapses in 2 and 10 month old homozygous mice. N = 234-433 synapses. Nonparametric Kruskal Wallis ANOVA with Dunn's multiple comparison test. (G) Number of synapses in dorsal and ventral tissue in 2 and 10 month old homozygous mice. N = 20-23 images. Nonparametric Kruskal Wallis ANOVA with Dunn's multiple comparison test. (H) Histogram of the number of GlyRs per synapse calculated from the molecular conversion of detections (see Fig. S4 and S5). N = 433 dorsal synapses and 304 ventral synapses. CV = coefficient of variation. (I) Scatter plot of GlyR density vs synapse area shows no difference between dorsal and ventral synapse densities. N = 433 dorsal synapses and 304 ventral synapses. *$p < 0.05$, **$p < 0.01$, ***$p < 0.001$.

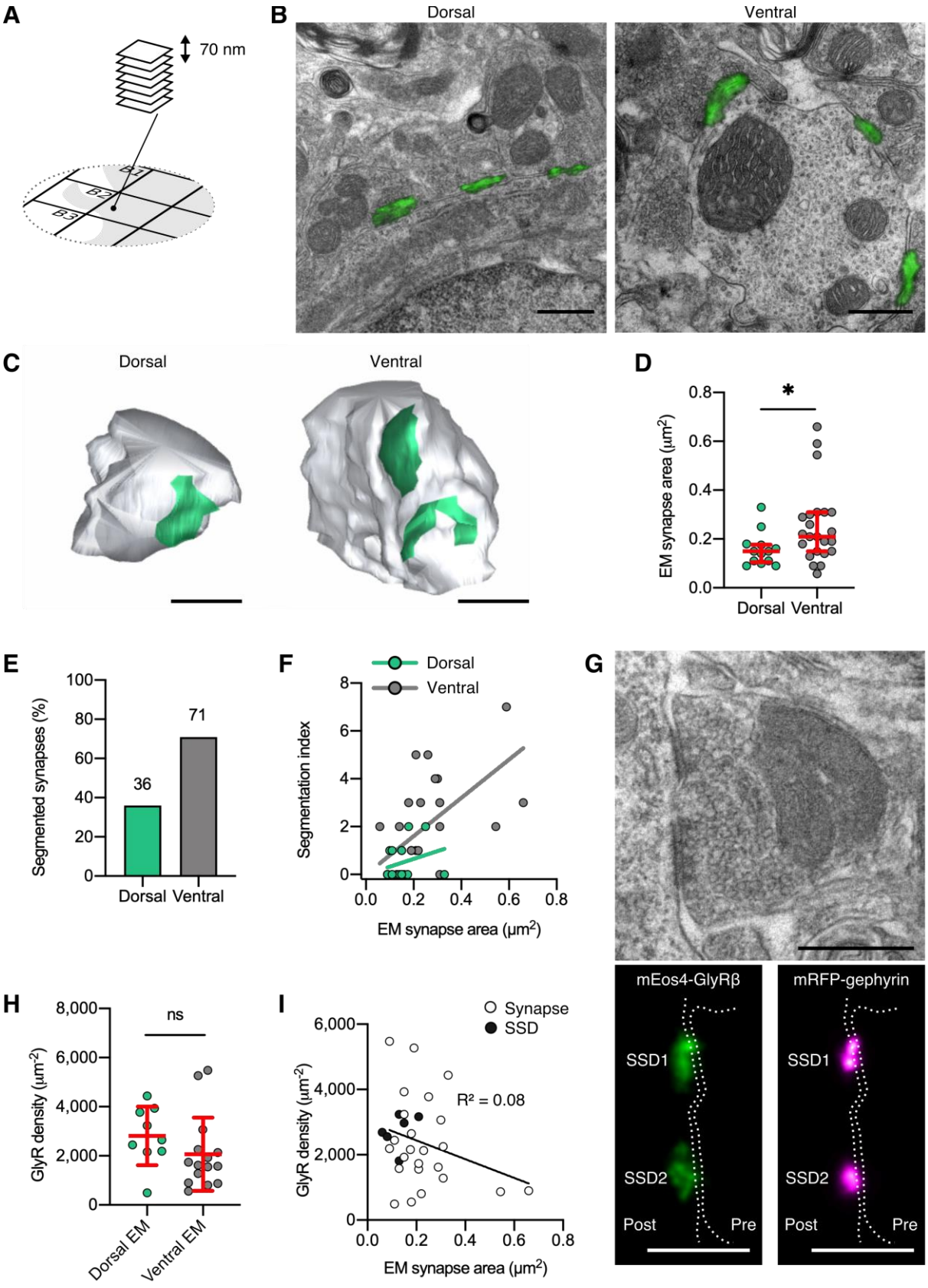


**Fig. 3. Quantitative SR-CLEM.** (A) Samples used for PALM were re-sectioned as serial ultra-thin 70 nm sections for CLEM. (B) Representative dorsal and ventral synapses imaged with PALM (green) and super-imposed with their corresponding electron micrographs. Scale bar = 500 nm. (C) Representative 3D reconstructions of dorsal and ventral synapses. Green =

PSD, gray = presynaptic bouton. Scale bar = 500 nm. (D) Area of dorsal and ventral synapses measured by EM. Nonparametric unpaired two-tailed t-test, Mann-Whitney post hoc. (E) Percentage of total synapses measured in EM with segmented shapes. (F) Comparison of segmentation index with synaptic area in dorsal and ventral synapses. (G) Juxtaposition of a raw electron micrograph and reconstructed PALM/SRRF images of sub-synaptic domains (SSDs) in the same ventral synapse. Scale bar = 500 nm. (H) Analysis of GlyR density following correction for EM area measurements. (I) Combined scatter plot of dorsal and ventral synapse densities shows density is independent of synapse size. White = all synapses, black = SSDs. N = 13 dorsal and 23 ventral synapses. *$p < 0.05$, ns = not significant.

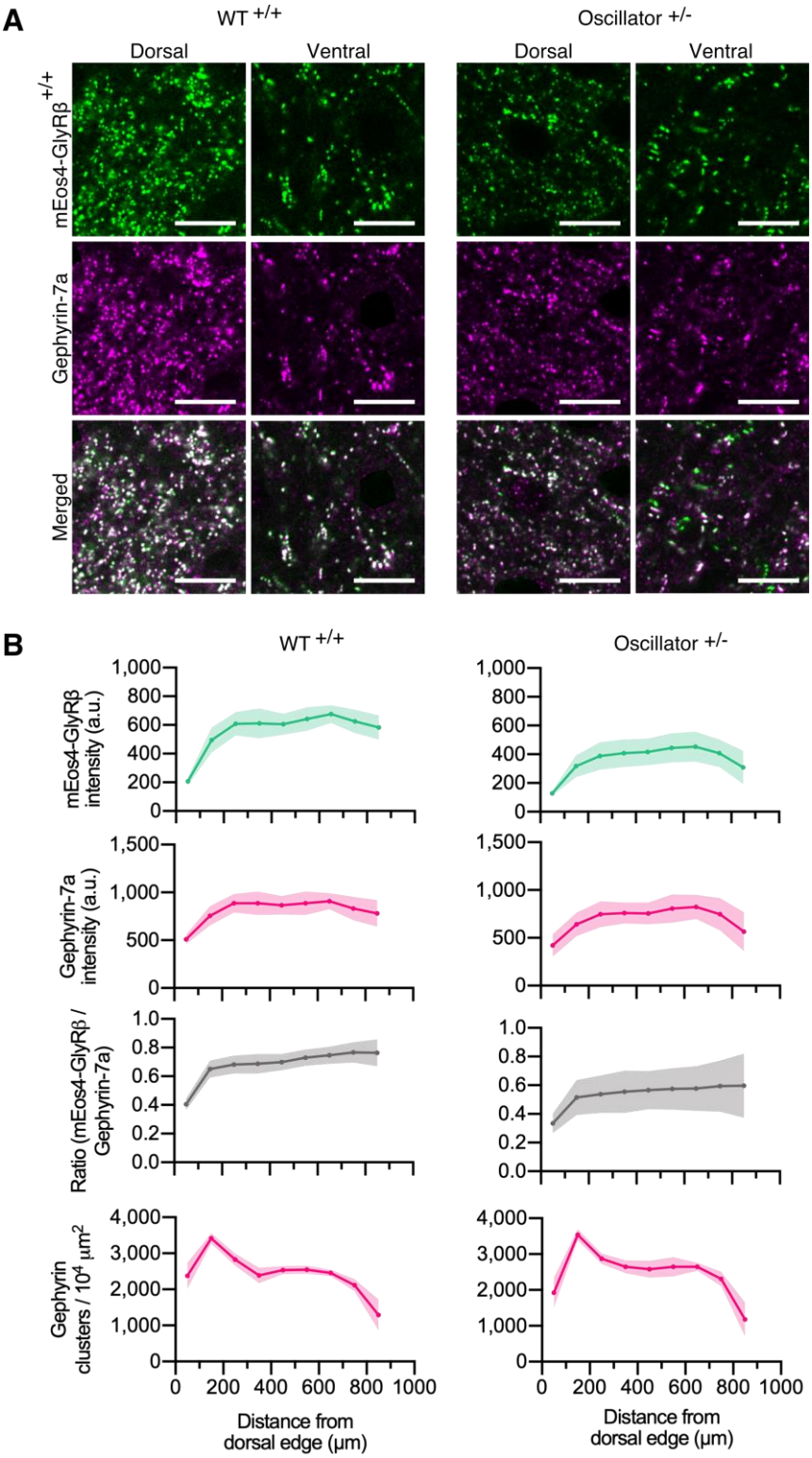


**Fig. 4. Quantitative confocal imaging of the *oscillator* mouse model.** (A) Representative confocal images of dorsal and ventral synapses from heterozygous *oscillator* mice (+/-) compared to homozygous WT (+/+) littermates. All mice are homozygous for mEos4b-GlyRβ (green), with gephyrin-7a immunolabeling (magenta). Scale bar = 10 µm. (B) Mean intensity ± 95% confidence interval of mEos4b-GlyRβ and gephyrin-7a at gephyrin-positive puncta, and numbers of gephyrin clusters measured from distal edge of spinal cord in 2 month old mice. N = 9-11 images per genotype.

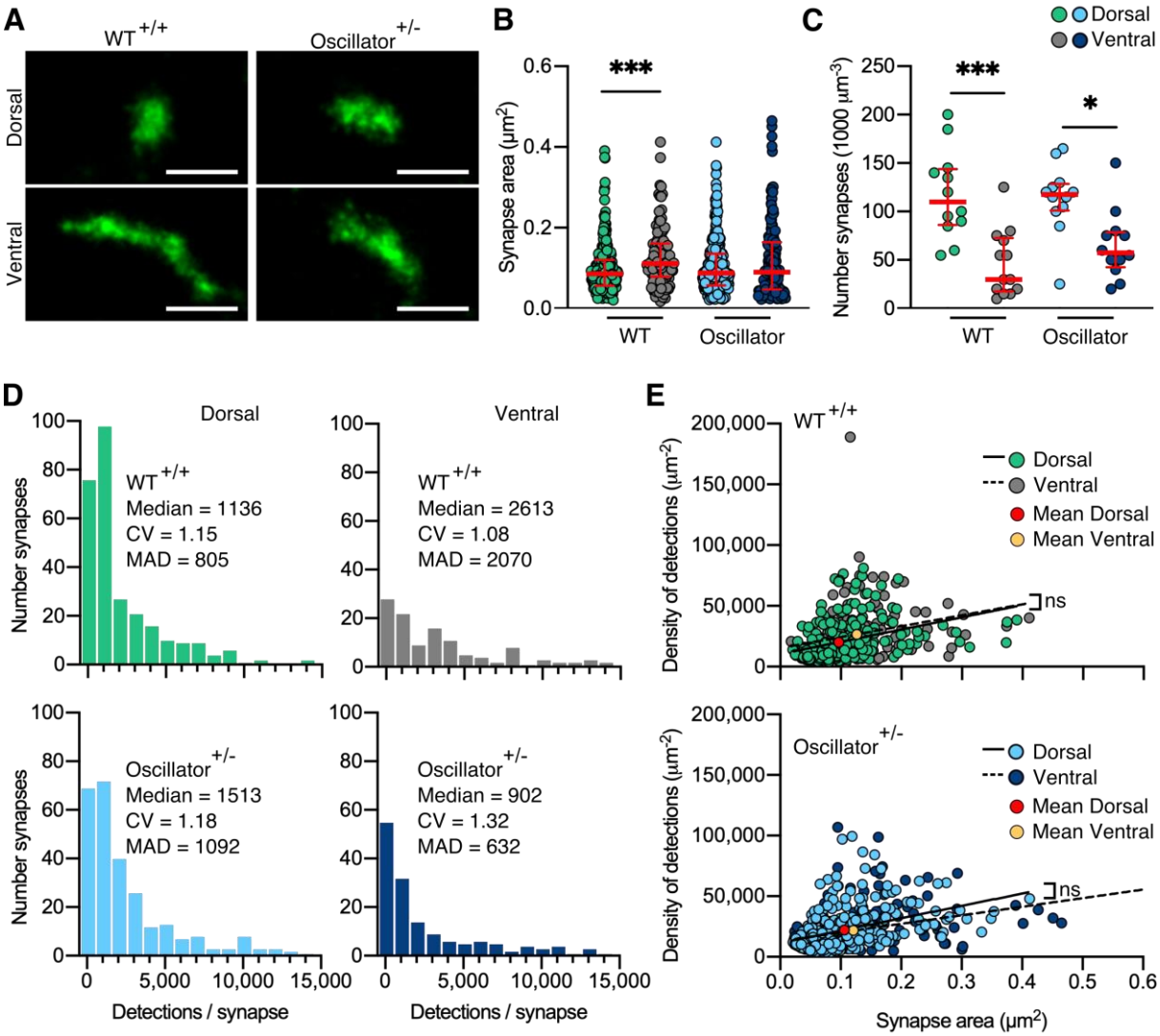


**Fig. 5. PALM imaging of the GlyR in the *oscillator* mouse model.** (A) Representative PALM reconstructions of mEos4b-GlyRβ at single dorsal and ventral synapses in heterozygous (+/-) *oscillator* and homozygous (+/+) WT littermates. Scale bar = 500 nm. (B) Area of dorsal vs ventral synapses in heterozygous *oscillator* vs WT littermates. N = 120-282 synapses. Nonparametric Kruskal Wallis ANOVA with Dunn's multiple comparison test. (C) Number of synapses in dorsal and ventral tissue in heterozygous *oscillator* vs WT mice. N = 12-13 images. Parametric one-way ANOVA with Tukey's multiple comparison test. (D) Histogram of the number of mEos4b detections per synapse. N = 282 WT dorsal and 120 ventral synapses, 273 *oscillator* dorsal and 156 ventral synapses. CV = coefficient of variation, MAD = median absolute deviation. (E) Scatter plots of mEos4 detection density vs synapse area shows no difference between dorsal and ventral synapse densities in *oscillator*. N = same as in (D). *p < 0.05, ***p < 0.001, ns = not significant.